SAND2021-14869C

Drop Interaction with a Conical Shock

Kyle A. Daniel*, Daniel R. Guildenbecher†, Paul M. Delgado ‡
Glen E. White§, Sam M. Reardon§ , H. Lee Stauffacher III¶, Steven J. Beresh‖
Sandia National Laboratories, Albuquerque, NM

This work presents an experimental investigation of the deformation and breakup of water drops behind conical shock waves. A conical shock wave is generated by firing a bullet at Mach 4.5 past a vertical column of drops with a mean initial diameter of 192 μm. The time-resolved drop position and maximum transverse dimension are characterized using backlit stereo videos taken at 500 kHz. A Reynolds-Averaged Navier Stokes (RANS) simulation of the bullet is used to estimate the gas density and velocity fields experienced by the drops. Classical correlations for breakup times derived from planar-shock/drop interactions are evaluated. Predicted drop breakup times are found to be in error by a factor of three or more, indicating that existing correlations are inadequate for the response to the three-dimensional relaxation of the velocity and thermodynamic properties downstream of the conical shock. Next, the Taylor Analogy Breakup (TAB) model, which solves a transient equation for drop deformation, is evaluated. TAB predictions for drop diameter calculated using a dimensionless constant of $C_2 = 2$, as compared to the accepted value of $C_2 = 2/3$, are found to agree within the confidence bounds of the ensemble averaged experimental values for all drops studied. These results suggest the three-dimensional relaxation effects behind conical shock waves alter the drop response in comparison to a step change across a planar shock, and that future models describing the interaction between a drop and a non-planar shock wave should account for flow field variations.

I. Introduction

The interaction of liquid drops with passing shock waves has been studied for many decades. When such interactions occur, drops are subjected to transient relative gas velocities and associated aerodynamic forces. If these aerodynamic forces are sufficiently greater than restorative surface tension forces, drops will deform and may eventually shatter into a cloud of finer drops.

A vast majority of prior experimental investigations consider planar shock waves generated in shock tubes. The works of Reinecke and Waldman [1–3] exemplify typical experiments. Using shadowgraphy and x-ray imaging in a shock tube to Mach numbers as high as 11 (reported more thoroughly in [4]), Reinecke and Waldman drew several empirical relationships that built on the foundational studies of Ranger and Nicholls [5], Engel [6], Nicholson [7], and others . Many subsequent authors (non-exhaustively, [8–16]) have added more data, some alterations to the empirical relationships, and further physical insights. However, for the most part, the basic empirical correlations have remained in general use for well over fifty years. Recent reviews are provided by Pilch and Erdman [13], Guildenbecher et al. [14], and Theofanous [15].

A drop subjected to relative gas conditions is typically characterized by the non-dimensional Weber number,

$$We = \frac{\rho_g u_g^2 d_o}{\sigma} \tag{1}$$

where ρ_g is the gas density, u_g is the relative gas velocity, d_o is the initial drop diameter, and σ is the interfacial surface tension. A great number of studies considering step changes in relative gas velocities have shown that a drop is generally unstable and will break up into a cloud of fine drops when the initial exceeds a critical value of around eleven [13, 14, 16]. The time over which breakup occurs often is nondimensionalized as suggested by Ranger and Nicholls [5],

$$T = \frac{t u_g}{d_o}\sqrt{\frac{\rho_g}{\rho_d}} \tag{2}$$

*Postdoctoral Appointee, Member AIAA, kadani@sandia.gov
†Principal Member of the Technical Staff, Engineering Sciences Center, Senior Member AIAA
‡Senior Distinguished Member of the Technical Staff, Engineering Sciences Center, Senior Member AIAA
§Electromechanical Technologist
¶Manager, R&D Science and Engineering
‖Distinguished Member of the Technical Staff, Engineering Sciences Center, Associate Fellow AIAA

American Institute of Aeronautics and Astronautics

where t is time, and ρ_d is the density of the liquid drop. For drops of relatively low viscosity and moderate *We*, (*We* $\lessapprox 10^4$), experimental observations such as the Reinecke and Waldman [1–3] suggest that drop breakup is complete by $T_{breakup} \approx 3.5$. Others have suggested $T_{breakup} \approx 5$, [5, 9, 16], whereas Pilch and Erdman [13] developed a more complex function of *We* meant to include effects of different breakup modes at smaller *We*. However, these differences may have little practical consequence given the typically large *We* found in shock tubes and the data scatter arising from experimental ambiguities

Many of these shock tube studies also sought to measure the deformation of a drop from its initial spherical shape. Reinecke and Waldman [1] added an empirical fit for deformation of the drop shape flattening into a disc as a function of T, showing monotonic growth of the cross-stream dimension for $T < 1.0$. Longer-time analyses by Ranger and Nicholls [5], Wierzba and Takayama [12], and Park et al. [17] all have shown an increase in cross-stream diameter until about $T = 1 - 2$, then a decrease as the breakup mode changes. Hsiang and Faeth [9] showed a monotonic diameter increase more akin to Reinecke and Waldman [1].

A more recent approach is known as the Taylor Analogy Breakup model (TAB) first proposed by O'Rourke and Amsden [18], which solves a differential equation for the cross-stream drop diameter rather than a purely empirical fit. The TAB model is based on Taylor's [19] analogy of a drop to a forced spring-mass-damper system where the force is the disruptive gas flow, the spring is the restorative surface tension, and the damper is the liquid viscosity. Here, we use the TAB formulation as provided by Hess et al. [20],

$$\frac{d^2y}{d\bar{t}^2} = -20Oh\frac{dy}{d\bar{t}} - 64(y-1) + 2C_2We. \tag{3}$$

where y can be interpreted as the nondimensional transverse drop dimension, d_c/d_o. The drop Ohnesorge number Oh is defined as,

$$Oh = \frac{\mu_d}{\sqrt{\rho_d d_0 \sigma}} \tag{4}$$

where μ_d is the liquid viscosity. In Eq. (3), C_2 is a dimensionless constant, which O'Rourke and Amsden [18] suggested $C_2 = 2/3$. Finally, $\bar{t}$ is time that has been made nondimensional by the drop natural oscillation frequency,

$$\bar{t} = \frac{t}{\sqrt{\rho_d d_0^3/\sigma}} \tag{5}$$

In a typical TAB simulation, a time and/or spatially varying gas velocity is provided by a Computational Fluid Dynamics (CFD) simulation. Within the CFD domain, an initially spherical drop ($y = 1$) is assumed to start at rest ($dy/d\bar{t} = d^2y/d\bar{t}^2 = 0$). The differential equation provided by Eq. (3) is solved along with formations for aerodynamic drag to predict the time and spatially resolved position and deformation of the drop. In the current work, the compressible drag relations of Parmar et al. [21] are used.

In many prior publications, the TAB model and several variants thereof [22–25] have been shown to provide reasonable predictive capability for applications to relatively low speed phenomena, such as liquid sprays. As suggested by Hess et al. [20], the TAB model may also be advantageous for predicting drop dynamics induced by shock wave interaction; although, prior to the current work, no experimental validation data was available. This motivates the current work to attempt the first known experimental validation of the TAB model for application to 3D drop dynamics induced by shock wave passage.

Most all of the prior experimental data and models have been developed using planar shock interactions as typically generated by a shock tube. This restriction to planar shocks has been tolerable because authors such as Reinecke and Waldman [1–4] and later Rodeman and Longcope [26] have generally considered effects near a nosetip, where the shock shape may be approximated by a planar shock. But farther from this region, drops will encounter a conical shock. Drop passage through this oblique shock may loosen the applicability of the relationships developed using planar shocks. This is not just an implication of the relatively weaker oblique shock, but also is influenced by the three-dimensional relaxation of velocity and thermodynamic properties downstream of a conical shock, whereas a planar shock induces a step change that does not relax following shock passage. This motivates the current effort to develop new experimental methods capable of directly quantifying 3D drop dynamics within conical shocks and downstream post-shock regions, then employing the resulting data to test models originally crafted for planar shocks or low-speed flows.

The current approach is to generate a conical shock wave by firing a high-velocity bullet past a column of falling water drops. This is conceptually similar to previous experiments that have used light-gas guns to launch projectiles at drops. However, such studies have been focused either on impact and material response (e.g., Moylan et al., [27], Lukasik et al. [28]) or drop behavior near a projectiles nosetip where the shock is nearly normal (e.g., Barber et al.

[29]). Here, the interest lies in the interaction of a conical shock with a drop, where a bullet is a means of achieving the desired gas-flow. By combining the high-speed imaging that has been used successfully in such gas gun experiments with drop tracking and morphology image analysis [30, 31], it is possible to quantitatively assess the drop response to the shock generated by bullet passage. The present study aims to evaluate such conical-shock/drop interactions against drop response relationships derived from planar-shock/drop interactions.

II. Experimental Methods

A. Ballistic Projectile Configuration

The morphology and breakup time of water drops exposed to the aerodynamic forces behind a conical shock wave are examined using the experimental setup shown in Fig. 1a. Here a conical shock wave is formed using a bullet fired towards a vertical column of water drops. Once exposed to the flow behind the conical shock, the drop behavior is studied using high-speed back-lit images from two cameras in a stereo configuration.

For each shot, a bullet is fired from a research grade rifle. The projectiles used are 0.22 caliber hollow point bullets that are hand pressed into cartridges filled with a precision measured quantity of propellant. A break screen upstream of the measurement volume provides a trigger signal to the cameras and pulsed diode laser light sources. In the measurement volume a vertical column of drops is formed using a piezo drop generator with 50μm orifice diameter, fed with distilled water from a syringe pump. When the bullet passes through the measurement volume the drop column is exposed to aerodynamic forces behind the projectile's conical shock wave. Here a stereo configuration is chosen to triangulate the three-dimensional position of the drops and track their relative location with respect to the passing projectile.

Images are recorded at 500 kHz and at a resolution of 250 × 400 pixels using two Shimadzu HPV-X2 high speed cameras. Each camera is backlit with Cavilux Smart pulsed diode lasers that have a wavelength of approximately 640±10 nm and a pulse width of 10 ns. To ensure uniform brightness in each image, diffusor plates are placed in from of each laser light source. Stereo images are calibrated using a Correlated Solutions calibration target and their software program, VIC-3D. The example image in Fig. 1b shows the drop column, the projectile, and the conical shock wave it generates. The image in Fig. 1c is taken at a time when the projectile has left the field of view and the deformation of the drops is clearly observed.

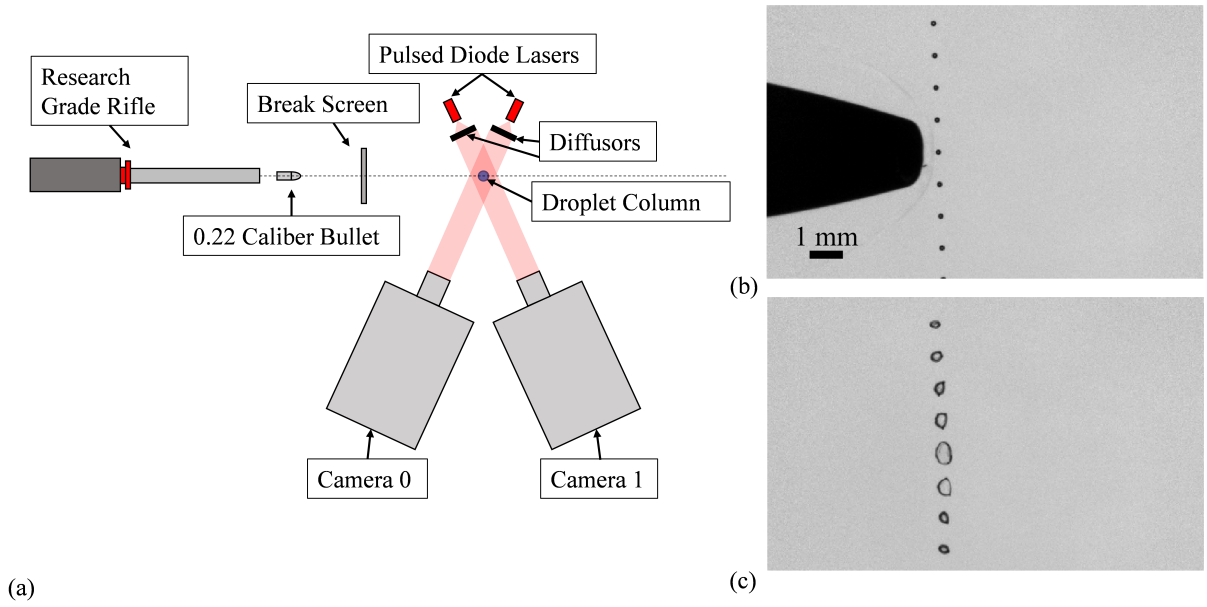

Figure 1. (a) Diagram of camera positions relative to bullet trajectory. Example images of moment (b) before bullet passes drop column and (c) after the bullet has passed out of frame and drop deformation has begun.

B. Drop and Bullet Tracking

The stereo video results represented in Fig.1b,c are post-processed to quantify time-resolved and three-dimensional (3D) bullet and drop trajectories and morphology using methodologies similar to our previous works [30–32] and briefly summarized here. To begin, dynamic thresholding defined in [30] is applied to each video frame in order to segment the dark objects from the lighter background. Next, two-dimensional (2D) object trajectories are constructed for each camera using the Regression-Based Multiframe Tracking (RMT) algorithm of [32]. Finally, triangulation methods in [31] are used to match the 2D trajectories between the stereo video pairs and quantify the 3D trajectory of each object.

Figure 2 shows example results. The first and second columns of Fig. 2 shows select image frames from the left and right camera, respectively, while the third column shows a triangulated view approximately normal to the video frames. Time between the frames shown in each row of Fig. 2 is $80\mu s$, while full trajectories are resolved at the video inter-frame time of $2\mu s$. The outlines shown in the Fig. 2 images show the measured drop regions with unique colors assigned to individual drops that are matched between the stereo pair and tracked over time. Spheres in the triangulated out-of-plane view correspond to individual drops and are similarly colored. Black vectors in Fig. 2 show instantaneous measured velocities (smoothed with a 15-frame rolling average for the Fig. 2 visualization). Finally, the dotted black circle in the out-of-plane view shows the outer diameter of the bullet centered at its triangulated position.

The mean flow induced by the bullet is axisymmetric. Consequently, the drop/bullet interaction is logically studied as a function of the relative axial and radial distances from the bullet tip. To find these dimensions, each component of the 3D triangulated positions of the bullet tip is first fit to a linear model with respect to time, yielding a constant value (zero acceleration) measurement of the bullet velocity vector. Next, the time resolved axial component of the relative drop to bullet position, $z(t)$, is found by

$$z(t) = (\vec{X}_d(t) - \vec{X}_b(t)) \cdot \vec{n}_b \tag{6}$$

where $\vec{X}_d(t)$ are the 3D triangulated drop positions in cartesian coordinates, $\vec{X}_b(t)$ are the 3D cartesian bullet positions extrapolated to all video frames using the best-fit linear models, and $\vec{n}_b$ is the unit vector corresponding to the measured bullet velocity vector. Similarly, the radial component of the relative drop to bullet position, $r(t)$, is found by

$$r(t) = \|\vec{A}(t) - (\vec{A}(t) \cdot \vec{n}_b)\vec{n}_b\| \tag{7}$$

where $\vec{A}(t)$ is a vector from the drop to a point on the line defining the bullet path, and the double lines signify the vector norm. Here, we choose $\vec{A}(t) = \vec{X}_d(t) - \vec{X}_b(t = t_{b0})$ where t_{b0} is the first frame for which the position of the bullet tip is triangulated.

Uncertainty in the 3D cartesian positions, $\vec{X}_d$ and $\vec{X}_b$, is assumed to be dominated by error in the 2D image centroids. This uncertainty is quantified by randomly offsetting the 2D image centroids by ± 1 pixel and retriangulating. From many such realizations, the typical standard deviation in triangulated positions is around $\pm 20\mu m$ along the horizontal and vertical coordinates that approximately align with the image plane in Fig. 2. As expected, typical uncertainty in the optical depth direction is larger at around $\pm 50\mu m$. Similarly, uncertainty in the measured bullet velocity and corresponding unit normal vector, $\vec{n}_b$, is found by randomly offsetting the 2D positions of the bullet tip by ± 1 pixel followed by retriangulating and refitting with linear models.

Uncertainty in the relative drop axial, $z(t)$, and radial, $r(t)$, positions is found by randomly offsetting the measured $\vec{X}_d$,$\vec{X}_b$, and $\vec{n}_b$ with Gaussian distributions matching the component standard deviations as found above and recalculating $z(t)$ and $r(t)$ from Eqs. 6 and 7, respectively. From many such realizations, the typical uncertainty in $r(t)$ is around $\pm 75\mu m$. Uncertainty in $z(t)$ starts at a similar level for video frames where the bullet is visible. Linear extrapolation of the bullet position (and associated uncertainty in $\vec{n}_b$) results in a constant increase in uncertainty in $z(t)$ up to a maximum of around 0.5 mm at the final video frames. Still, this is only a small fraction of the typical interframe bullet axial displacement of around 3 mm.

Finally, the time resolved drop dimensions are measured from the segmented 2D drop regions as shown in Fig. 2. First the triangulated optical depth is combined with knowledge from the stereo camera calibration to determine the effective magnification and pixel pitch, Δx, of the left and right cameras. For the example shown in Fig. 2, the magnified pixel pitch at the optical depths of the segmented drop regions is around Δx =37 and $35\mu m$ for the left and right cameras, respectively. At frames before arrival of the bullet, the initial drop diameter, d_0, is found from

$$d_0 = \Delta x \sqrt{\frac{4N_{pixels}}{\pi}} \tag{8}$$

where N_{pixels} is the number of pixels in the segmented drop region. As the drop deforms following passage of the bullet, d_0 becomes less meaningful. Instead, deformed drops are quantified by their maximum transverse dimension, d_c, found by

$$d_c = \Delta x H_{pixels} \tag{9}$$

where H_{pixels} is the largest dimension of the rotated rectangular bounding box that encloses the segmented drop region. Both the left and right cameras give measured values of d_0 and d_c. Here, the mean of the left and right values is reported as the measured value.

Uncertainty in measured drop dimensions is likely affected by several factors including uncertainties due to stereo camera calibration, pixelized segmentation, view angle limitations, and others. A comprehensive analysis of these uncertainties is beyond the scope of the current work. Instead, uncertainty in d_0 and d_c is simply estimated from the standard deviation of the absolute value of the difference between the quantities measured by the left and right cameras. For the Fig. 2 results, this gives an estimated uncertainty in drop diameters of around 30 to 70μm, which is equivalent to 1 to 2 pixels of uncertainty.

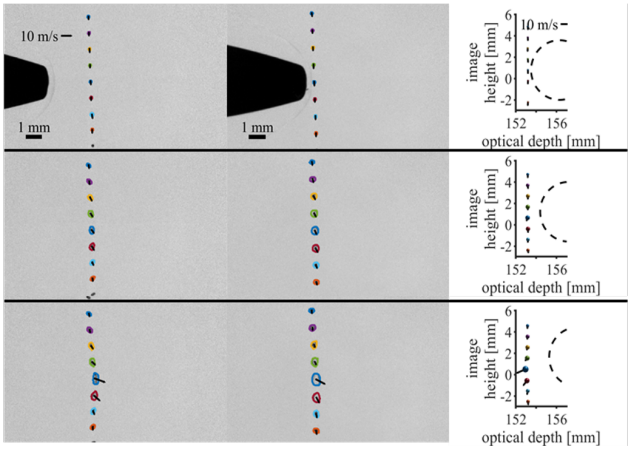

Figure 2. Example 3D triangulated drop and bullet results.

C. RANS Flowfield

The flow conditions induced by the bullet passage are not easily measured during the experiments, nor are they generally predictable from theory. Quantities of interest include the gas density and velocity fields through which the drops pass, as both parameters are found in the existing correlations for drop response discussed in the introduction and are required for TAB simulations. To estimate these quantities, computational simulations were conducted of the bullet flight.

Reynolds-Averaged Navier Stokes (RANS) simulations were conducted using the Sandia Parallel Aerodynamics and Reentry Code (SPARC). The computational simulations were realized for the supersonic ideal gas flow using a second-order Steger-Warming Inviscid flux scheme with a generalized minmod flux limiter, a weighted least-squares gradient scheme, and a second order adaptive CFL-controlled time stepping scheme with a maximum CFL of 20,000. The Spallart-Allmaras turbulence model was initialized with a turbulent viscosity factor of 3.0 (with reference length 1.0).

The computational mesh for the bullet geometry was extracted from 3D scans of the bullet and post-processed to extract the axisymmetric outer mold line of the surface while removing the hollow tip. Simulations that included the hollow tip proved much more computationally expensive, difficult to converge due to the unsteady cavity flow, and ultimately did not prove significant to the present application at radial distances away from the nosetip. A structured hexahedral mesh was fitted to the bullet and wake with a maximum equiangle skewness 0:54, minimum wall angle of 68°, and maximum $Y+$ of 10 to enhance capturing of turbulent wake effects. The wake region was extended twenty bullet lengths to ensure capture of the gas dynamics downstream of the bow shock.

Figure 3 compares experimental schlieren images of the 0.22-caliber bullet to synthetic schlieren generated from the RANS simulation. Near the bullet nose the RANS simulation captures the shape of the bow shock and weak expansion wave shown in the experimental schlieren. At radial distances away from the bullet, some spatial attenuation of the simulated shock is evident due to numerical dissipation. Towards the aft end of the bullet, both the RANS and

experimental schlieren show weak expansion and compression waves that originate from the groove in the bullet. Further downstream of the bullet a recompression shock forms. Here the RANS simulations correctly predict the angle of the compression wave, suggesting simulations adequately capture the flowfield further downstream of the bullet in areas outside of the bullet wake. In summary, favorable overall agreement between the experiments and simulations in Fig. 3 indicates that the RANS simulations adequately capture the main flow features and are therefore suitable for prediction of relative gas properties as needed to interpret experimental drop behavior and perform TAB modeling in the next section.

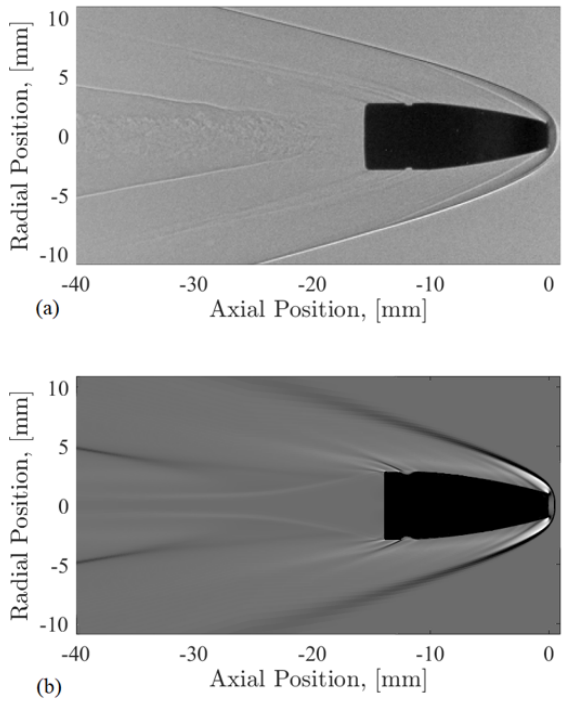

Figure 3. (a) Schlieren image of a high-velocity bullet. (b) Synthetic schlieren from a RANS simulation of the bullet flowfield at Mach 4.5

III. Results & Discussion

A. Example Drop Response

Figure 4 summarizes a typical experimental result. This example corresponds to the drop that displays the most significant deformation and breakup in Figs. 1 and 2 (fifth drop from the top, with blue outline in Fig. 2). The first and second row of Fig. 4a show zoomed-in portions of the left and right camera frames, respectively. The relative gas velocity components are shown in the first plot on the bottom in Fig. 4b. Values shown are the RANS predicted gas velocity components at the measured axial and radial position of the drop with respect to the bullet minus the measured drop velocity components. Similarly, the middle plot in Fig. 4c shows the RANS predicted local gas density along the measured drop trajectory. These quantities are combined with the measured initial drop diameter, $d_0 = 192\mu$m, to estimate the temporal history of the drop Weber number, *We*, shown in Fig. 4d. Finally, in Fig. 4 and the rest of this discussion $t = 0$ is defined as the instant when the leading shock wave first crosses the drop's location, based on the RANS predicted shock structure.

The Fig. 4 data reveal the dynamic nature of this problem. As shown in Fig. 4b the relative gas velocities rise sharply upon passage of the conical shock. This is followed by a 5 μs period of gradual decline and then a second rapid transient as the flow induced by the groove and the recompression wave pass over the drop. After about 15μs, rapid transients cease, and gas velocities in the wake gradually return to quiescent values. At the same time, Fig. 4c shows that the local gas density also varies rapidly. Immediately after the primary shock, densities are several times greater than ambient. However, for much of the subsequent interaction time, the gas density is sub-ambient. Finally, in Fig. 4d, these variations in both the gas velocities and densities combine via Eq. (1) to predict a rapid decrease

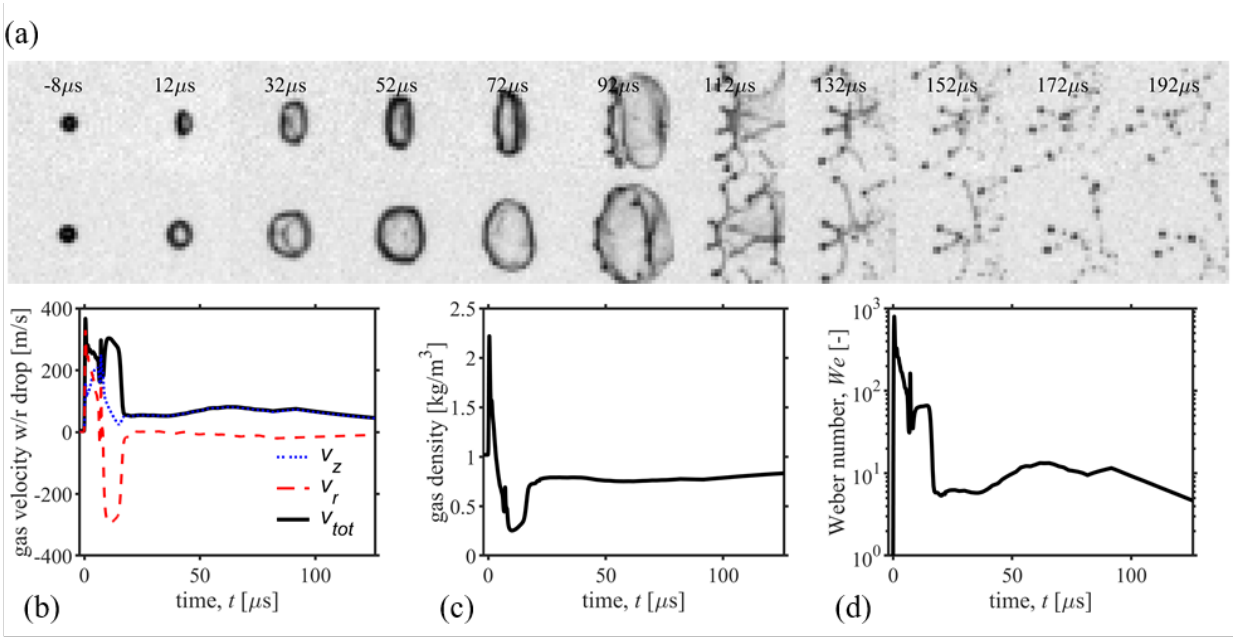

Figure 4. Example 3D triangulated drop and bullet results showing the (a) drop deformation and the temporal variation of the (b) gas velocity (c) density, and (d) Weber number experienced by the drop.

in the relative *We* from its initial peak value of around 800 immediately after the shock passage to less than 10 in the wake.

B. Comparison to Uniform Flow Conditions

With such rapid transients, a key question to be answered by the present experiment is: Can classical shock-tube correlations based on step changes in relative gas properties describe the likelihood of drop breakup behind a conical shock? Of course, this question raises the immediate challenge of selecting characteristic values for nondimensionalization. Whereas shock-tube studies can straightforwardly define singular values for *We* and nondimensional time based on the step change across the planar shock, the much more dramatic temporal variation in relative gas properties seen in Fig. 4, owing to the three-dimensional relieving effect behind a conical shock, does not lend itself to simple choices for characteristic quantities.

In an analogous manner to the step change across a planar shock, one might consider defining characteristic gas properties based on peak values immediately after the drop crosses the conical shock. As a reliable indicator for when the drop crosses the conical shock, in this work we use the instant when the drop experiences its maximum predicted *We*. With RANS predicted u_g and ρ_g at this instant, time can also be nondimensionalized via Eq. (2). Nondimensionalization using this choice of characteristic gas quantities is referred to here as "peak *We*" and is analogous to similar prior suggestions made by Reinecke and Waldman [1–3].

As discussed in the introduction, classical shock tube correlations suggest that drop breakup is complete at a nondimensional time of around $T_{breakup} \approx 3.5$ to 5. For the example shown in Fig. 4, the use of characteristic gas properties from the peak *We* predicts a total breakup time between 39 to 56μs. In contrast, the experimentally observed breakup time from the images in the top of Fig. 4 is $\approx 150\mu s$. Therefore, in this example, the use of peak shock properties predicts a total breakup time that is approximately 3x too fast compared to experiments.

As seen in Fig. 4, conditions immediately after the shock are short lived. To make better use of prior correlations we might hope to use characteristic gas properties at some later time. Unfortunately, there is no obvious best choice of time to define these properties. As one possible example, here we consider the time at which breakup appears to "initialize". In the current work, we use the Pilch and Erdman [13] definition of "initiation" as the instant in the experimental videos when child drops are first observed to be shed from the main drop. For the example shown in Fig. 4, initiation occurs at roughly 100μs, at which point the drop is well downstream of the bullet. Using gas properties at this instant, the classical shock tube correlations predict a total breakup time of between 360 to 520μs. This is now approximately 3x too slow compared to the experimental breakup time. Clearly, these simple attempts to apply

classical shock tube correlations are inadequate for this example.

To statically quantify these observations, Fig. 5 show nondimensionalization by the "peak *We*" and "initiation time" criteria for all drops quantified in the current experiments. Of the 128 drops, only 9 reached complete breakup in the 256μs of the image sequences, while about twice as many began initial breakup. Characteristic nondimensional values for these cases are denoted by the symbols in Fig. 5. Drops that remain intact throughout the duration of the video are labeled as such in Fig. 5. For these data points, nondimensional time is simply the latest time in the video sequence and therefore the drops may remain intact to much longer times. Although this definition of intact time is arbitrary, data points are nevertheless included to demonstrate the scatter in the nondimensional Weber number of drops that do not break apart.

Overall, Fig. 5 results provide little meaningful predictive capability for either selection of characteristic gas properties. When conditions are nondimensionalized using gas properties from the peak *We* in Fig. 5a, all nondimensional times are above the dotted green line at $T_{breakup} \approx 3.5$ suggested by shock-tube experiments. This indicates that for all drops considered in the current experiment, the use of shock-tube correlations based on the conditions at the peak *We* would predict breakup times that are significantly faster than reality. The opposite can be observed when conditions are nondimensionalized using conditions at initiation as shown in Fig. 5b. There, all data points are now below the breakup time suggested by shock-tube experiments. This indicated that for all drops considered in the current experiment, the use of shock-tube correlations at conditions based on this later time would predict breakup at significantly slower rates than reality.

Regardless of which nondimensionalization scheme is used, the data points for breakup do not consistently distinguish themselves from intact drops. Intact drops tend to cluster along a curve that represents the values for *We* and T at the end of an image sequence, but many drops in a stage of breakup coexist along this curve. Similarly, most of the cases experiencing breakup fall at lower values of T, which reflects the earlier times at which this occurs, but a number of intact drops can be found in this region of the plots as well. Therefore, not only do the two nondimensionalization schemes presented in Fig. 5 predict breakup either faster or slower than reality, but they fail to predict which drops should remain intact and which should breakup.

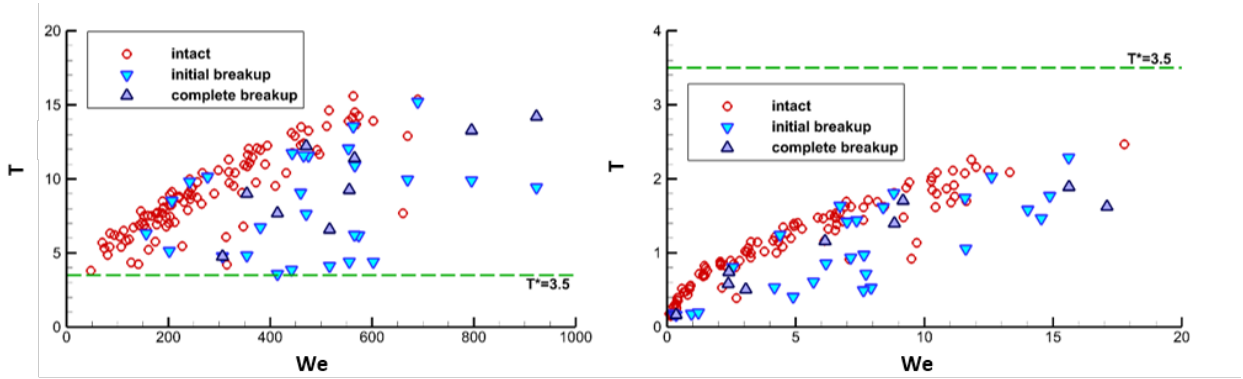

Figure 5. Nondimensional Weber numbers and breakup times when characteristic gas properties are selected at (a) the peak *We* values immediate after the shock and (b) the drop initiation time.

Therefore, Fig. 5 demonstrates that shock tube correlations for drop breakup at $T_{breakup} \approx 3.5$ to 5 are not a reasonable approximation for drop breakup across a conical shock. The additional three-dimensional relieving effects certainly alter the drop response in comparison to a step change across a planar shock. It is perhaps possible that some complex means of determining *We* and T for the changing conditions caused by three-dimensional relief could provide better agreement with the $T_{breakup} \approx 3.5$ to 5 criterion, but none has been discovered herein nor is suggested by the known literature on the subject.

Additionally, the empirical drop deformation relationships derived from uniform flow conditions in shock tubes can be tested against the present conical-shock data. Both Reinecke and Waldman [1–3] and Ranger and Nicholls [5] provide empirical relations of the transverse drop dimension d_c as a function of T. These relationships presently are tested against the measured d_c for drops that remained intact to the end of the image sequence and nondimensionalized by the peak *We* values as in Fig. 5a. In all cases, the rate of drop deformation is greatly overpredicted, much as Fig. 5a overpredicts the rate at which drops will breakup. These correlations are too simplistic to represent drop deformation response across a conical shock with three-dimensional relaxation.

C. TAB Model Predictions

The prior section demonstrated that classical shock-tube correlations for step changes in relative velocity are inadequate for prediction of drop dynamics in the present flow. As discussed in the introduction, the TAB model [18] and its derivatives [22–25] solves a transient equation for drop deformation, and, as such, has potential to better predict dynamics observed in the rapidly varying flow field downstream of the conical shock. Quantifying the predictive capabilities of the TAB model is the goal of this section.

TAB simulations of experimentally measured drops are initialized at axial and radial locations and velocities matching the experimentally measured values immediately before arrival of the shock. Similar to the implementation discussed in [20], the TAB equation for drop deformation, Eq. (3), is solved simultaneous with Lagrangian drop tracking, including variable drag coefficients due to deformation. At each time step, local gas velocities and densities are interpolated from the RANS solution (Fig. 3). Equations are solved in MATLAB using the explicit Runge-Kutta formulation. In the current implementation, drop breakup into child drops is not simulated. Consequently, TAB predictions are likely invalid after drops begin to display complex morphologies and breakup.

Figure 6 shows TAB predictions for the example drop shown in Fig. 4. Here, times up to $50\mu s$ are shown. This time roughly corresponds with the experimental time in Fig. 4 where the complex bag morphology is first observed and after which time the TAB model is no longer applicable. The left plot in Fig. 6 compares the measured drop axial, $z(t)$, (blue dots, left axis) and radial, $r(t)$, (red squares, right axis) positions with corresponding TAB predictions (dotted blue and red lines, respectively). In this case, the change in axial and radial positions is almost entirely determined by the bullet trajectory. Therefore, as expected, predicted positions closely match the measured values and all predictions fall within the experimental uncertainty bounds shown by the error bars in Fig. 6. (Note the change in scales between the left and right axes. Differences between the measured and predicted drop radial positions are less than 0.1 mm.)

The right plot in Fig. 6 shows the measured drop cross-steam diameter, d_c, as grey circles with error bars quantifying experimental uncertainty. TAB predictions for several values of the constant, C_2, are shown by the dotted, colored lines. In their original derivation, O'Rourke and Amsden [18] suggest $C_2 = 2/3$, and most subsequent applications of the TAB model, including a recent attempt to apply TAB to a computational flow configuration similar to the current [20], have used $C_2 = 2/3$. Still, some prior researchers have observed better agreement with different values of C_2 e.g., Schmehl [22]. Indeed, the results in Fig. 6b indicate that a higher value of C_2 ($C_2 \approx 2$ better predicts the measured deformation.

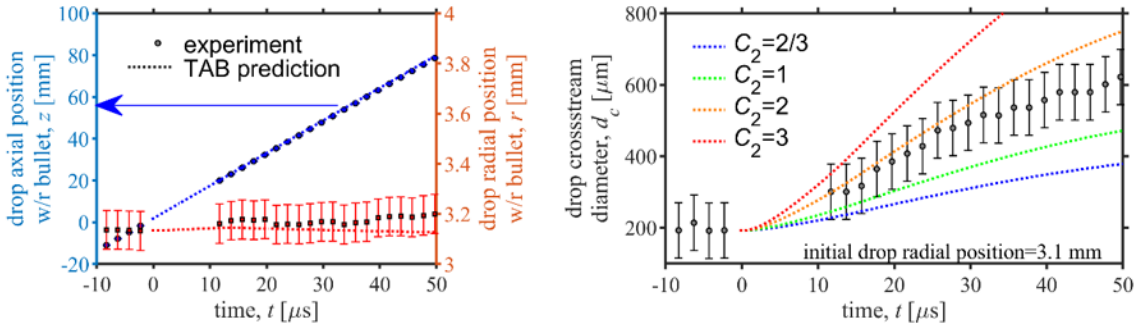

Figure 6. Taylor Analogy Breakup (TAB) model prediction applied to the example drop in Fig. 4

To consider the predictive capability of the TAB model across a broader range of conditions, we next consider all other drops in the single experimental realization shown in Fig. 1 and 2. Figure 7 shows the time history of *We* for all eight drops in this experimental shot. Line colors and the arrow in Fig. 7 correspond with drops at increasing radial distances from the bullet. As expected, the peak *We* monotonically decreases when the drop is radially further away from the bullet. This suggests that a single experimental shot can provide a relatively broad range of aerodynamic loading conditions that are well sorted by the initial radial distance from the bullet center line.

Next, Fig. 8 shows TAB model predictions of drop deformation corresponding with four other select drops from the realization shown in Fig. 1 and 2. Note, the initial drop radial position shown in the lower right of each sub-figure. As expected, the extent of the drop deformation decreases with increasing radial distance from the bullet centerline. Importantly, for all drops shown in Fig. 8 TAB predictions corresponding to $C_2 \approx 2$ agree within the experimental uncertainty bands for most of the times shown in Fig. 8.

Finally, to statistical quantify model accuracy, Fig. 9 presents ensemble averages of experimental data and corresponding TAB predictions for all 25 shots and 128 drops. Each subplot in Fig. 9 is constructed from all drops that

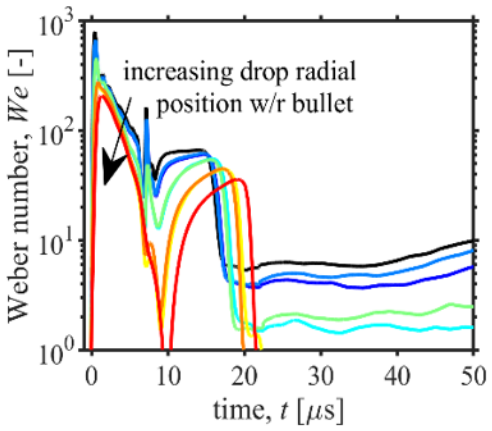

Figure 7. Temporal variation in Weber number for all drops corresponding to the experimental realization of Fig. 1 and 2. Note, black line is the example drop in Fig. 4.

fall within the range of initial radial positions shown in the upper right. Grey circles show the ensemble average of the experimental d_c/d_0. Here, error bars are the 95% confidence intervals of the mean (not experimental uncertainty of individual measurements as in prior figures). In addition, because the actual drop radial positions vary within the range shown of each subplot in Fig. 9, the predicted aerodynamic loading also has some variation, as do the resulting TAB predictions. In Fig. 9 the ensemble averaged mean TAB predictions are shown as solid lines, while dotted lines show $\pm$ 1 standard deviation of the TAB predictions.

In all Fig. 9 results, the TAB model predictions corresponding to C_2 =2 agree within the confidence bounds of the ensemble averaged experimental values. In addition, further TAB modeling was performed for C_2 values ranging from 1 to 3 in increments of 0.25, and the minimum root mean square error in d_c/d_0 between experiments and simulations was used to quantify the optimum C_2 value. This analysis indicates that the optimum C_2 is 2$\pm$0.25 for the entire range of experimental conditions considered in this work.

Provided that some *a priori* information is available to inform selection of C_2, Fig. 9 results indicate that the TAB model is a promising technique for prediction of drop deformation induced by the rapidly varying flows behind the conical shock. Unfortunately, however, an adequate explanation for why C_2 must be increased compared with the value of 2/3 suggested by O'Rourke and Amsden [18] is not current available. Note, in Eq. (3), C_2 is the constant of proportionality associated with the disruptive aerodynamic force in Taylor's [19] spring-mass-damper analogy. O'Rourke and Amsden's [18] value of C_2 was selected based on observations from classical shock-tube experiments. Perhaps for the conic shock conditions, a higher C_2 is necessary to capture the integrated effects of the rapidly vary aerodynamic forces, especially at early times. Still, this explanation is unproven and far from adequate. Further work is certainly warranted. Finally, several authors have proposed improvements and derivatives of the classical TAB model considered here. Examples include the works in [22–25] and others listed in Hess et al. [20]. Each of these models should certainly be investigated to determine if any are more predictive or may require have less reliance on ad hoc parameter turning. Nonetheless, the TAB model offers a reasonable early-time deformation prediction of drops subjected to a conical shock passage

IV. Conclusion

The interaction between a liquid drop and a conical shock was studied by firing a bullet near a vertical column of drops. The diameter, position, and breakup time of the drops were examined using backlit stereo videos of the conical-shock/drop interaction.

Classic shock tube-based correlations for breakup time were evaluated. In these shock tube-based relations, a non-dimensional time is defined by the constant gas properties behind a planar shock. In the case of a conical shock, the gas relaxes, leading to variations in the velocity field and thermodynamic properties behind the shock wave. To evaluate these classic correlations, a non-dimensional breakup time is calculated using the gas properties at times associated with the peak Weber number and the time at which drop breakup is initiated. In both cases the correlations predict breakup times that are in error by a factor of three or more. This demonstrates that the three-dimensional flow field

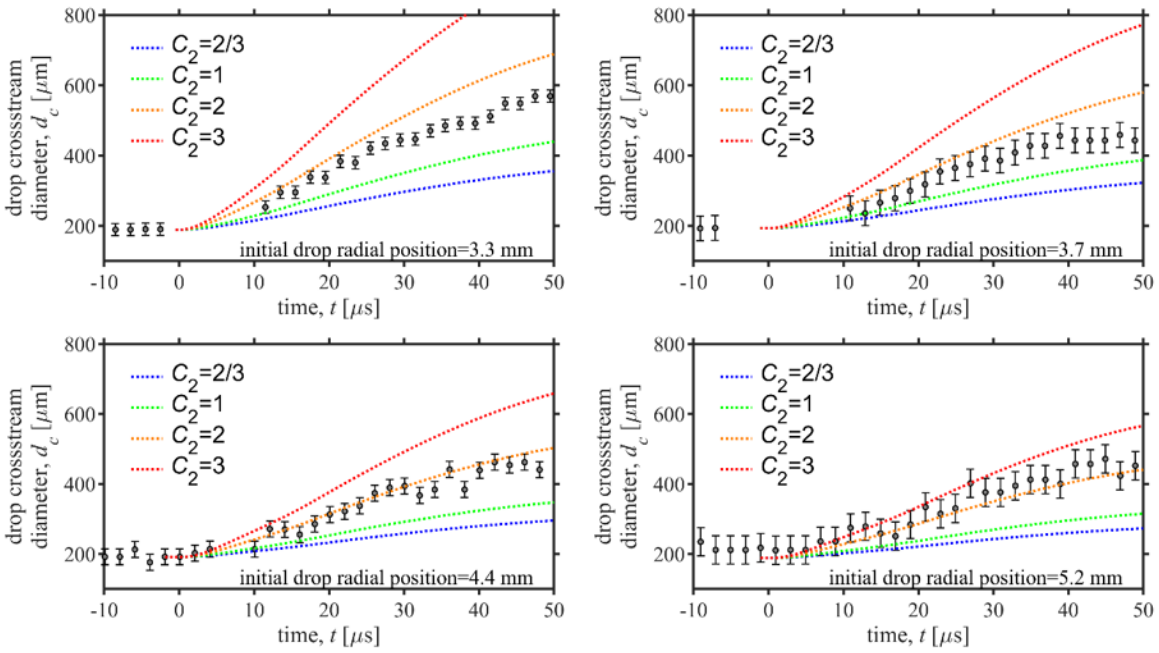

Figure 8. Taylor Analogy Breakup (TAB) model predictions of drop deformation for four example drops from the experimental shot in Fig. 1 and 2.

behind conical shocks alters the drop response in comparison to a step change across a planar shock and indicates a need for correlations that account for flow field variations.

The Taylor Analogy Breakup (TAB) model is examined as a potential method to estimate drop deformation behind a conical shock. Because the TAB model solves a transient equation for drop deformation it has potential to better predict drop dynamics observed in the varying flow field downstream of the conical shock. TAB predictions for drop diameter are found using various values of the constant C_2. A value of $C_2 = 2$ was found to agree within the confidence bounds of the ensemble averaged experimental values for all drops studied. This suggest with *a priori* knowledge of the approximate C_2 value, the time varying deformation of drops behind a conical shock wave can be estimated. However, in the original derivation of the TAB model, O'Rourke and Amsden [18] found a constant of $C_2 = 2/3$ best fit experimental data from drop breakup. While the larger value of C_2 found in the current study may be related to the rapidly varying gas quantities behind a conical shock, a more conclusive reason for this discrepancy has yet to be determined.

Overall, the data presented here indicate the need for better tools to predict drop dynamics behind a conical shock. The classical TAB model examined in this study shows great promise in the capacity and indicates that the proposed improvements to the TAB model present in the literature [22–25] should be investigated. Experimental methods and results presented here should be useful for validation of future models of this environment.

Acknowledgments

The authors would like to thank Harlan Brown-Shaklee and Jon Eberhart for their helpful guidance towards application relevance.

Sandia National Laboratories is a multi-mission laboratory managed and operated by National Technology and Engineering Solutions of Sandia, LLC., a wholly owned subsidiary of Honeywell International, Inc., for the U.S. Department of Energy's National Nuclear Security Administration under contract DE-NA0003525.

References

[1] Reinecke, W. and Waldman, G., "A study of drop breakup behind strong shocks with applications to flight," Tech. rep., Force Report SAMSO-TR-70-143, May 1970.

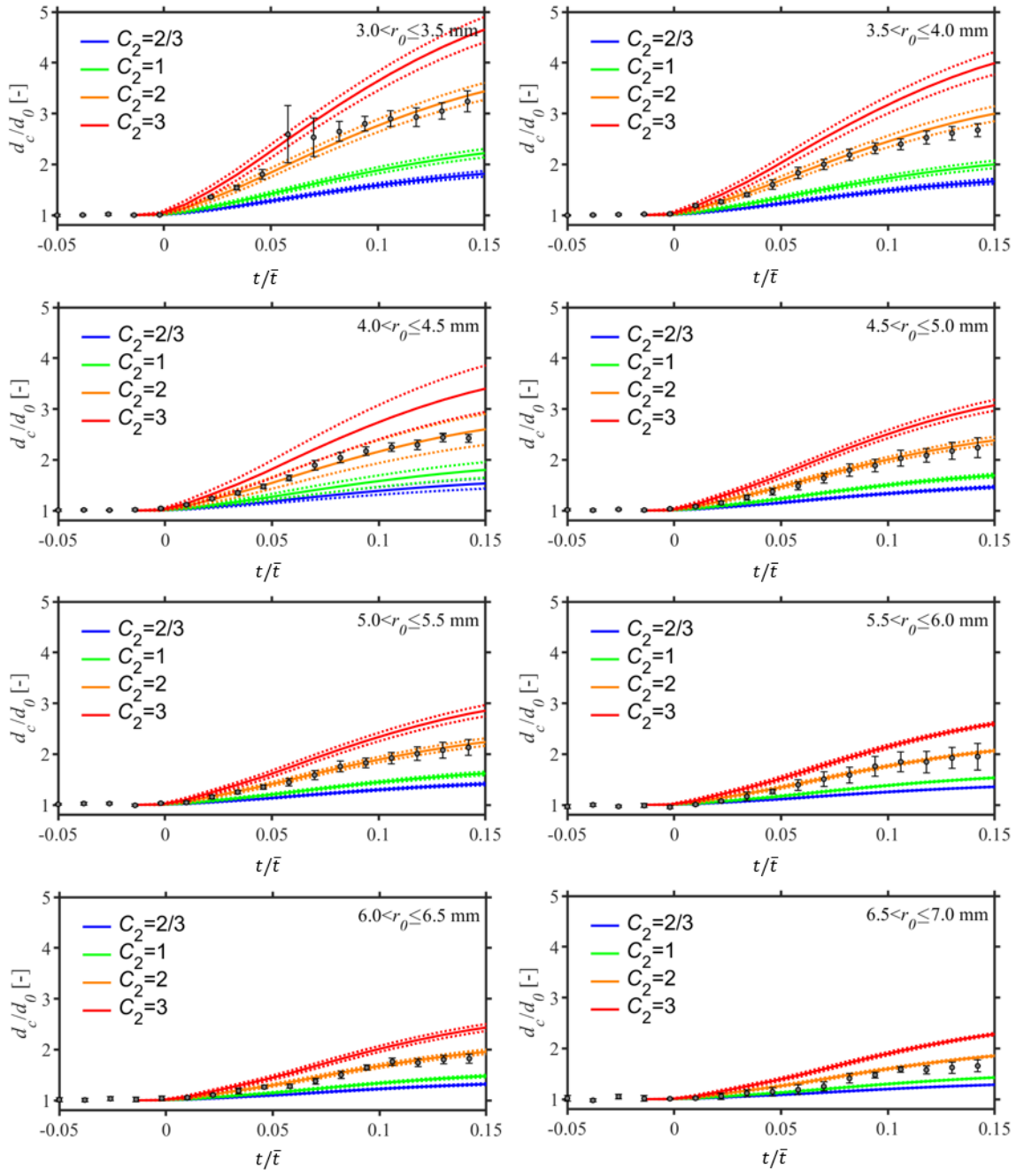

Figure 9. Ensemble averages of experimental measures (grey circles) and Taylor Analogy Breakup (TAB) model predictions (colored lines) of drop deformation from all 128 individual drops measured in experiments.

[2] Reinecke, W. and Waldman, G., "An investigation of water drop disintegration in the region behind strong shock waves," *3rd Int. Conf. on Rain Erosion and Related Phenomena, Hampshire, England*, 1970.

[3] Waldman, G. D., Reinecke, W. G., and Glenn, D. C., "Raindrop breakup in the shock layer of a high-speed vehicle," *AIAA journal*, Vol. 10, No. 9, 1972, pp. 1200–1204.

[4] Reinecke, W. and McKay, W. L., "EXPERIMENTS ON WATER DROP BREAKUP BEHIND MACH 3 TO 12 SHOCKS." Tech. rep., Sandia Report SC-CR-70-6063p, 1969.

[5] Nicholls, J. and Ranger, A., "Aerodynamic shattering of liquid drops." *Aiaa Journal*, Vol. 7, No. 2, 1969, pp. 285–290.

[6] Engel, O. G., "Fragmentation of waterdrops in the zone behind an air shock," *J. Res. Natl. Bur. Stand*, Vol. 60, No. 3, 1958, pp. 245–280.

[7] Nicholson, J. E., "Drop breakup by airstream impact," Tech. rep., RAE Report N68-19401-427, 1968.

[8] Simpkins, P. and Bales, E., "Water-drop response to sudden accelerations," *Journal of Fluid Mechanics*, Vol. 55, No. 4, 1972, pp. 629–639.

[9] Hsiang, L.-P. and Faeth, G. M., "Near-limit drop deformation and secondary breakup," *International journal of multiphase flow*, Vol. 18, No. 5, 1992, pp. 635–652.

[10] Chou, W.-H., Hsiang, L.-P., and Faeth, G., "Temporal properties of drop breakup in the shear breakup regime," *International Journal of Multiphase Flow*, Vol. 23, No. 4, 1997, pp. 651–669.

[11] Joseph, D. D., Belanger, J., and Beavers, G., "Breakup of a liquid drop suddenly exposed to a high-speed airstream," *International Journal of Multiphase Flow*, Vol. 25, No. 6-7, 1999, pp. 1263–1303.

[12] Wierzba, A. and Takayama, K., "Experimental investigation of the aerodynamic breakup of liquid drops," *AIAA journal*, Vol. 26, No. 11, 1988, pp. 1329–1335.

[13] Pilch, M. and Erdman, C., "Use of breakup time data and velocity history data to predict the maximum size of stable fragments for acceleration-induced breakup of a liquid drop," *International journal of multiphase flow*, Vol. 13, No. 6, 1987, pp. 741–757.

[14] Guildenbecher, D., López-Rivera, C., and Sojka, P., "Secondary atomization," *Experiments in Fluids*, Vol. 46, No. 3, 2009, pp. 371–402.

[15] Theofanous, T., "Aerobreakup of Newtonian and viscoelastic liquids," *Annual Review of Fluid Mechanics*, Vol. 43, 2011, pp. 661–690.

[16] Theofanous, T., Li, G., Dinh, T.-N., and Chang, C.-H., "Aerobreakup in disturbed subsonic and supersonic flow fields," *Journal of Fluid Mechanics*, Vol. 593, 2007, pp. 131–170.

[17] Park, G., Yeom, G.-S., Hong, Y. K., and Moon, K. H., "Experimental Study of Time-Dependent Evolution of Water Droplet Breakup in High-Speed Air Flows," *International Journal of Aeronautical and Space Sciences*, Vol. 18, No. 1, 2017, pp. 38–47.

[18] O'Rourke, P. J. and Amsden, A. A., "The TAB method for numerical calculation of spray droplet breakup," Tech. rep., SAE Technical Paper, 1987.

[19] Taylor, G. I., "The shape and acceleration of a drop in a high speed air stream," *The scientific papers of GI Taylor*, Vol. 3, 1963, pp. 457–464.

[20] Hess, A., Kessler, D. A., Johnson, R. F., Aguilera, C., Sosa, J., and Goodwin, G. B., "Evaluation of Droplet Aerodynamic Breakup Models in Supersonic and Hypersonic Flows," *AIAA Scitech 2021 Forum*, 2021, p. 0751.

[21] Parmar, M., Haselbacher, A., and Balachandar, S., "Improved drag correlation for spheres and application to shock-tube experiments," *Aiaa Journal*, Vol. 48, No. 6, 2010, pp. 1273–1276.

[22] Schmehl, R., "Advanced modeling of droplet deformation and breakup for CFD analysis of mixture preparation," *Zaragoza*, Vol. 9, No. 11, 2002.

[23] Park, J.-H., Yoon, Y., and Hwang, S.-S., "Improved TAB model for prediction of spray droplet deformation and breakup," *Atomization and sprays*, Vol. 12, No. 4, 2002.

[24] Ibrahim, E., Yang, H., and Przekwas, A., "Modeling of spray droplets deformation and breakup," *Journal of Propulsion and Power*, Vol. 9, No. 4, 1993, pp. 651–654.

[25] Tanner, F. X., "Liquid jet atomization and droplet breakup modeling of non-evaporating diesel fuel sprays," *SAE transactions*, 1997, pp. 127–140.

[26] Rodeman, R. and Longcope, D., "Rain-induced vibration," *AIAA Journal*, Vol. 21, No. 3, 1983, pp. 459–465.

[27] Moylan, B., Landrum, B., and Russell, G., "Investigation of the Physical Phenomena Associated with Rain Impacts on Supersonic and Hypersonic Flight Vehicles," *Procedia Engineering*, Vol. 58, 2013, pp. 223–231.

[28] Rogers, J., Mead, P. T., Harrison, K., Kota, K. R., Leaverton, J. D., Lukasik, G., Kulatilaka, W. D., Wilkerson, J. W., and Lacy, T. E., "Hypervelocity Impact Response of Polyethylene Plates," *AIAA Scitech 2021 Forum*, 2021, p. 0887.

[29] Barber, J. P., Grood, E. S., Taylor, H. R., and Hopkins, A. K., "Water Drop/Bow Shock Interactions." Tech. rep., AFML-TR-75-105, 1975.

[30] Guildenbecher, D. R., Gao, J., Reu, P. L., and Chen, J., "Digital holography simulations and experiments to quantify the accuracy of 3D particle location and 2D sizing using a proposed hybrid method," *Applied optics*, Vol. 52, No. 16, 2013, pp. 3790–3801.

[31] Guildenbecher, D. R., Olles, J. D., Miller, T. J., Reu, P. L., Yeager, J. D., Bowden, P. D., and Schmalzer, A. M., "Characterization of Hypervelocity Fragments and Subsequent HE Initiation." Tech. rep., Sandia National Lab.(SNL-NM), Albuquerque, NM (United States), 2018.

[32] Guildenbecher, D. R., Cooper, M. A., and Sojka, P. E., "High-speed (20 kHz) digital in-line holography for transient particle tracking and sizing in multiphase flows," *Applied optics*, Vol. 55, No. 11, 2016, pp. 2892–2903.